Meta-tensegrity: design of a tensegrity prism with metal rubber

Yanhong Ma[1], Qicheng Zhang[1], Yousef Dobah[2], Fabrizio Scarpa[2,a], Fernando Fraternali[3], Robert E. Skelton[4], Dayi Zhang[1], Jie Hong[1]

[1]School of Energy and Power Engineering, Beihang University (BUAA), Beijing, 100191, P.R. China
[2]Bristol Composites Institute (ACCIS), University of Bristol, University Walk, BS8 1TR Bristol, UK
[3]Department of Civil Engineering, University of Salerno, 84084 Fisciano, Italy
[4]Aerospace Engineering, Texas A&M, College Station, TX 77843-3141, USA

Abstract

A tensegrity structure involves the presence of elements withstanding pure compression, and others under pure tension only. Metal rubber is introduced into a tensegrity prism strut to create a mechanical metamaterial with energy absorption and tuneable dynamic properties. In this work we describe the design and development of the meta-tensegrity structure with particular emphasis on the evaluation of parameters such as the structural size, the metal rubber stiffness, the initial internal force and the external compression load. Prototypes of tensegrity prisms with and without metal rubber inserts have been assembled and subjected to quasi-static loading. The model used to design the meta tensegrity prism has been then modified to take into account specific manufacturing and internal dissipation mechanisms typical of this configuration. The updated model provides a better comparison with the experimental results. Both the theoretical and experimental data show that the introduction of the metal rubber within the tensegrity configuration contributes to improve significantly the energy absorption, and to reduce the stiffness of the whole tensegrity structure.

1. Introduction

Tensegrity defines a family of reticulated space structures, initially conceived and presented in the form of sculptures during the 1940s by Fuller and Snelson[1,2]. Later, during the ‘70s the formal definition of tensegrity was termed as a set of discontinuous compressive elements interacting with a set of discontinuous tensile elements that

[a] Corresponding Author: f.scarpa@bristol.ac.uk

maintain a self-stressed stable volume in space [3]. Because the elements within a tensegrity structure are either in pure compression or pure tension with no bending or shear, the individual components and the whole tensegrity structure can be extremely lightweight [4,5]. Tensegrity also has other benefits, such as compact storage, robustness to failure, deployability and unique modes of locomotion [6]. Wave dynamics [7,8] and structural reinforcements for masonry [9] are also some of the peculiar aspects that tensegrity can fulfill.

Research activities and applications of tensegrity have been initially focused in architecture [1], and then extended to full scale deployable tensegrity wing [4] and a deployable station-keeping buoy [4]. Besides, due to their deployability and light weight, tensegrity systems have also been applied to space structures [10,11,12]. As an example, a deployable antenna reflector has been designed for ESA by Zolesi and Ganga [11]. That reflector is represented by a tensegrity ring with 12 bars, with a deployed diameter of 12m and a stowed one of 1.2m. Tensegrity robots [13] that can roll [14] or crawl [15] over rugged environments because of their deformation have also been recently evaluated. NASA's SunSpiral and Gorospe have developed a tensegrity-based probe for planetary exploration [6], which could be able to operate on Titan as a mobile lander with a science payload mass fraction of 50% compared to 18% of the Mars Exploration Rovers, and 22% of the Mars Science Laboratory. Although the probe appears to be sufficiently robust to be used as a landing platform, no apparent intrinsic damping that could absorb the impact and vibration and reduce the damage during landing is present within the tensegrity configuration.

In this paper we describe the design and testing of a tensegrity prism with internal metal rubber (MR) inserts assembled within the struts (compressive elements) [16]. MR is a class of innovative porous damping materials with high energy absorption capabilities, made of entangled metal wire by mold compression [17]. Metal rubber could operate in harsh environments with ambient temperatures ranging between -100℃ to 200℃ [18,19,20]. This temperature interval is compatible with deep space and planetary landing probes missions. Metal rubber is characterized by the presence of tunable microstructural deformation mechanisms that involve stick-slip contacts and generated

friction depending upon the level of entanglement, type of alloy used and the amplitude of the external dynamic loading [21,22]. As a multifunctional smart material, metal rubber has also been developed in shape memory metal [21,23], magnetostrictive [24,25] and even auxetic versions [26].

Mechanical metamaterials have been developed mainly by focusing on the use of lattice configurations exhibiting unusual deformation mechanisms [27,28,29], bi-or multi-material composites[30 , 31], and architectures with global/local deformation mechanisms providing combinations of negative material properties[32]. Metal rubber has also already been used as a part of structural platform in a mechanical metamaterial represented by a nonlinear vibration damper with auxetic characteristics [26].

The paper described the design, modelling and mechanical testing of a tensegrity prism with metal rubber inserts for potentially enhanced energy absorption capabilities. The paper is divided in 5 parts. The first is related to the development of a theoretical model of the tensegrity configuration with MR. Since the purpose of this paper is to study the influence of the MR presence in the tensegrity topology, the simplest tensegrity prism structure has been adopted (3 bars and 9 strings), therefore avoiding the use of form finding [33] and complex deforming analysis theories [4] for complex tensegrity structures. The model has then been used to perform a parametric analysis for the design of the prototypes. Details of the construction of two tensegrity configurations, one with metal rubber and another without are then presented. A section has been devoted to describe the quasi-static compressive tests, their results and discussions. The modification of the original tensegrity theoretical model based on the outcome of the experimental tests is discussed in the final section.

2. Theoretical model

2.1 Tensegrity prism without metal rubber

The tensegrity prism mechanical model can be established using a force equilibrium approach, rather than energy or dynamic relaxation methods [34], which are mostly used in more complex tensegrity structures. The theoretical description of the tensegrity prism without the MR inserts is mostly based on the model developed by Fraternali *et*

al [35].

The configuration of a regular tensegrity prism is illustrated in Fig. 1. The tensegrity consists of six nodes, three bars (in red color), three cross strings (in blue) and six horizontal strings (black). The three bars have the same length ***b***, while the length of the three cross strings is ***s*** and the six horizontal strings are of the same length ***l***. The six horizontal strings could be separated into two sets (bottom strings 1-2-3 and top strings 4-5-6). Each of them forms an equilateral triangle rotated with respect to each other by $\boldsymbol{\theta}$ (Fig. 1).

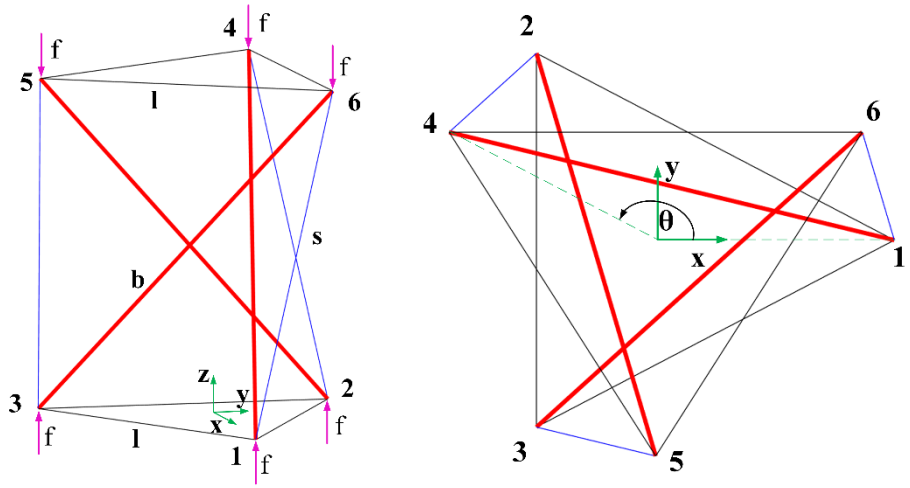

Fig. 1 Configuration of a regular tensegrity prism, 3D view left and top view right

The nodal vectors are expressed as:

$$\mathbf{n}_1=\begin{bmatrix}\frac{l}{\sqrt{3}}\\0\\0\end{bmatrix};\ \mathbf{n}_2=\begin{bmatrix}-\frac{l}{2\sqrt{3}}\\\frac{l}{2}\\0\end{bmatrix};\ \mathbf{n}_3=\begin{bmatrix}-\frac{l}{2\sqrt{3}}\\-\frac{l}{2}\\0\end{bmatrix};\ \mathbf{n}_4=\begin{bmatrix}\frac{l\cos\theta}{\sqrt{3}}\\\frac{l\sin\theta}{\sqrt{3}}\\h\end{bmatrix};\ \mathbf{n}_5=\begin{bmatrix}-\frac{l\sin\theta}{2}-\frac{l\cos\theta}{2\sqrt{3}}\\\frac{l\cos\theta}{2}-\frac{l\sin\theta}{2\sqrt{3}}\\h\end{bmatrix};\ \mathbf{n}_6=\begin{bmatrix}\frac{l\sin\theta}{2}-\frac{l\cos\theta}{2\sqrt{3}}\\-\frac{l\sin\theta}{2\sqrt{3}}-\frac{l\cos\theta}{2}\\h\end{bmatrix} \quad (1)$$

In (1), ***h*** is the prism height. The bar length ***b*** and cross string length ***s*** can both be expressed as a function of the prism height ***h***, the horizontal string length ***l*** and the twist $\boldsymbol{\theta}$ as:

$$b=\sqrt{h^2-\frac{2}{3}l^2\cos\theta+\frac{2l^2}{3}}$$
$$s=\sqrt{\frac{3h^2-\sqrt{3}l^2\sin\theta+l^2\cos\theta+2l^2}{3}} \tag{2}$$

It is evident from (2) that the topological structure of the tensegrity prism can be completely described by the three parameters ***h***, ***l*** and ***θ***. In any node of the tensegrity prism, the force equilibrium equations along the three Cartesian directions can be expressed in the following manner:

$$\begin{aligned} g_1&=\frac{1}{6}l\left[2\sqrt{3}\left(x_1+3x_2-x_3\right)+\sqrt{3}\left(x_1+2x_3\right)\cos\theta-3x_1\sin\theta\right]=0\\ g_2&=\frac{1}{6}l\left[\sqrt{3}\left(x_1+2x_3\right)\sin\theta+3x_1\cos\theta\right]=0\\ g_3&=h\left(x_3-x_1\right)-\frac{F}{3}=0 \end{aligned} \tag{3}$$

Where x_1, x_2 and x_3 denote the forces per unit length acting in the cross string, the horizontal string and the bar attached to the node. The definition of x_1, x_2 and x_3 is expressed as:

$$\begin{aligned} x_1&=\frac{F_s}{s}=\frac{k_1\left(s-s_N\right)}{s}\\ x_2&=\frac{F_l}{l}=\frac{k_2\left(l-l_N\right)}{l}\\ x_3&=\frac{F_b}{b}=\frac{-k_3\left(b-b_N\right)}{b} \end{aligned} \tag{4}$$

In (4), s_N, l_N and b_N are the natural lengths of the cross and horizontal strings and bars. The forces per unit length x_1, x_2 and x_3 are assumed to be positive when the strings are stretched and the bars compressed. The force F in equations (3) and (4) refers to the force acting on the tensegrity prim along the z-direction.

When there is no external force (F=0) only the twist $\theta=5/6\pi$ can provide stability to the prism [35], and therefore the self-stressed configuration of the tensegrity prism without an external force can be determined. This implies that any pair of self-stressed element length s_0, l_0, b_0 or h_0 can be obtained by the other pair using (2).

By substituting (4) in (3) the force equilibrium equations of the tensegrity prism under an external compression force along the z-direction can be rewritten as:

$$g_1 = 0 = \frac{l}{6}\left[4k_3 \sin^2\left(\frac{\theta}{2}\right)\left(\sqrt{3} - \frac{3b_N}{\sqrt{3h^2 - 2l^2\cos\theta + 2l^2}}\right) + k_1\left(-3\sin\theta + \sqrt{3}\cos\theta + 2\sqrt{3}\right) + k_2\frac{6\sqrt{3}\left(l - l_N\right)}{l} - k_1\frac{3s_N\left(-\sqrt{3}\sin\theta + \cos\theta + 2\right)}{\sqrt{3h^2 - \sqrt{3}l^2\sin\theta + l^2\cos\theta + 2l^2}}\right] \quad (5)$$

$$g_2 = 0 = \frac{l}{6}\left[2k_3 \sin\theta\left(\frac{3b_N}{\sqrt{3h^2 - 2l^2\cos\theta + 2l^2}} - \sqrt{3}\right) + k_1\left(\sqrt{3}\sin\theta + 3\cos\theta\right) - k_1\frac{3s_N\left(\sin\theta + \sqrt{3}\cos\theta\right)}{\sqrt{3h^2 - \sqrt{3}l^2\sin\theta + l^2\cos\theta + 2l^2}}\right]$$

$$g_3 = 0 = -\frac{F}{3} + k_3 h\left(\frac{b_N}{\sqrt{h^2 - \frac{2}{3}l^2\cos\theta + \frac{2l^2}{3}}} - 1\right) + k_1 h\left(\frac{\sqrt{3}s_N}{\sqrt{3h^2 - \sqrt{3}l^2\sin\theta + l^2\cos\theta + 2l^2}} - 1\right)$$

Equations (5) consist again of 3 equilibrium equations with 3 unknown parameters (***h***, ***l*** and ***θ***).

2.2 Metal rubber mechanical properties

The geometrical parameters of metal rubber samples used is listed in Table. 1. The MR specimens was produced using a nickel based superalloy wire with a diameter of 0.12mm, whose chemical compositions are listed in Table. 2. The manufacturing process of MR includes coiling of wire, weaving and folding of coiled wire, and finally molding by a compression force between 20kN and 60kN [21,36]. The compression loading is tailored to generate a specific porosity for the specimens, which is 0.28 in this paper. A CT(computed tomography) scan figure of MR specimen is shown in Fig. 2. It is possible to evince from the 3D image the high interconnectivity existing within the porous structure between wires, and the presence of connective micropores between tangled wires.

Table. 1 Parameters of MR specimen

Material	Porosity	Height	Diameter	Wire diameter
Nickel based superalloy	0.72	40mm	20mm	0.12mm

Table. 2 Chemical compositions (wt%) of the wire

Fe	Ni	C	Si	Mn	S	P	Cr
Balance	52.26	0.032	0.13	0.06	0.005	0.005	18.89
Mo	Al	Nb	Ti	Cu	Co	B	Mg
3.04	0.41	5.05	0.95	0.05	0.01	0.004	0.001

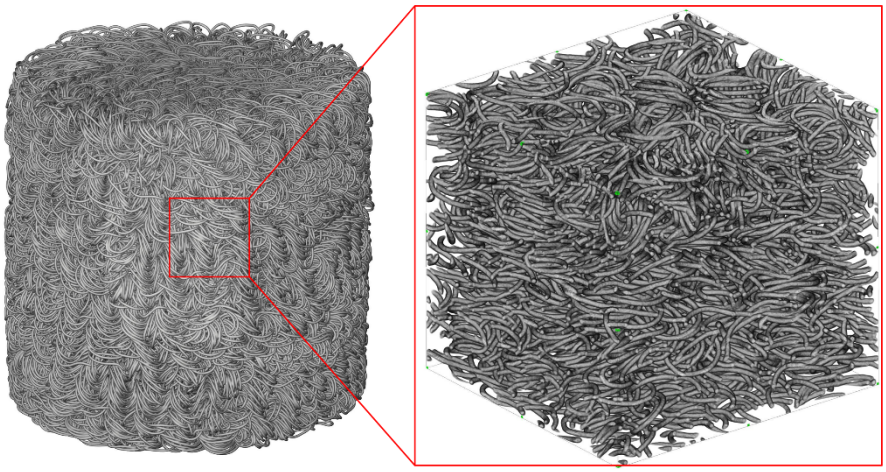

Fig. 2 CT image of metal rubber

Due to the presence of dry friction and stick-slip contacts within the metal rubber microstructure [36] the MR bar stiffness k_3 in equations (4) is nonlinear. It should also be noted that the k_3 used in equation (4) is a secant stiffness, which is defined by the total compression force over the total deformation.

To obtain the MR stiffness a series of quasi-static experiments has been carried out. The tests were performed using an electro-hydraulic SHIMADZU tensile with 1 kN load cell capacity (Fig. 3). The test was conducted by force control, with the loading and unloading rates at 1N/s.

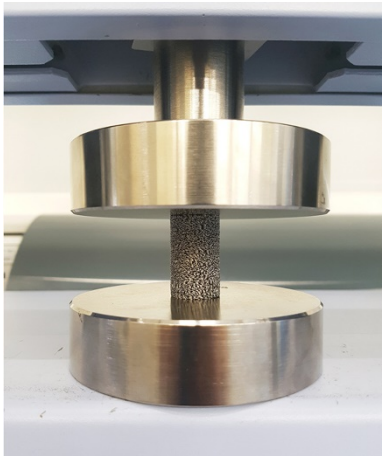

Fig. 3 Quasi-static test of the MR specimen

The hysteretic loop of the MR specimen during the first few test cycles were not consistent with each one [36]. During the first loading cycles the shape of the top and bottom surfaces of the MR specimen was not uniform, and stabilized after the 4^{th} cycle, when the repeatability of the hysteresis loops was adequate [36]. As a consequence, the

test results shown in Fig. 4 are referred to the ones from the average of the 4th cycles from 3 different MR specimens.

The main difference between the hysteresis provided by the cyclic loading at different pre-compression levels is represented by the unloading part of the curves. The peak force is provided by the 0 N pre-compression (~ 500 N), while the different pre-compression levels give similar maximum peak forces (~ 460N). The pre-compression decreases significantly the stroke available to the samples during the deformation (7.6 mm for 0N, decreasing to 3.4 mm for the 60 N case).

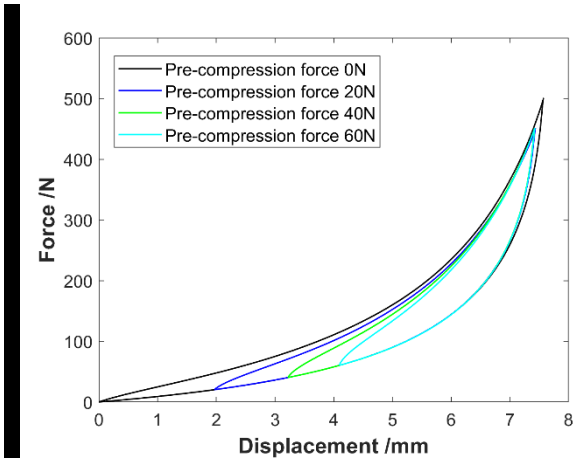

Fig. 4 Hysteretic loops of the MR specimen at different loading conditions

The loading and unloading secant moduli of the MR under different pre-compression forces are shown in Fig. 5. The behavior of the secant modulus may appear peculiar, as the loading curve at different pre-compression levels is not continuous, and the loading and unloading curves before pre-compression overlap with each other. The reason behind this behavior is because the stiffness formulation used in equations (4) requires that the secant modulus is calculated as total compression force (i.e., including the pre-compression) over total compression displacement (including the pre-compressed deformation). This means that, although the MR always works in the pre-compression after assembled into the tensegrity prism, the secant modulus used during the simulation should be considered calculated from its natural (pristine) length.

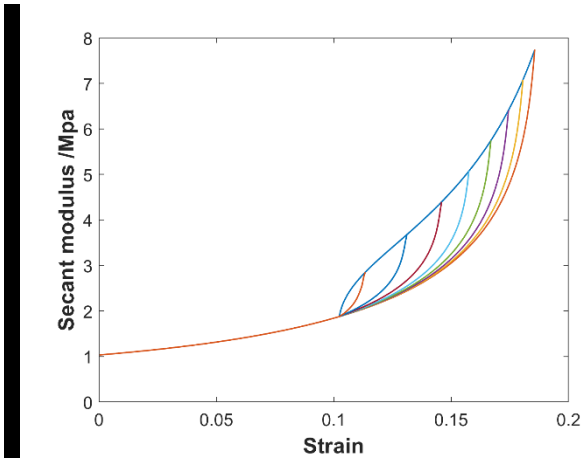

Fig. 5 Secant modulus of the MR specimen with a pre-compression of 60N at different cycles

The loss factors of the different hysteretic loops in Fig. 4 can be calculated based on the dissipated energy over the averaged loading and unloading energy [36]. The calculated loss factors are listed in Table. 3. It is apparent that the loss factor decreases with the increase of the maximum compression force, but exhibits a slight increase for higher pre-compression levels. As a broad range, the loss factors of the MR specimens vary between 0.15 and 0.17.

Table. 3 Loss factors of MR specimen in different loading and unloading conditions

Pre-compression force	Maximum compression force before unloading							
	450N	400N	350N	300N	250N	200N	150N	100N
20N	0.148	0.152	0.156	0.159	0.162	0.165	0.168	0.170
40N	0.151	0.155	0.159	0.162	0.166	0.169	0.173	0.173
60N	0.152	0.156	0.159	0.163	0.167	0.170	0.173	0.159

2.3 Model of the tensegrity prism with MR

The secant stiffness k_3 in equations (4) can be derived directly from the secant modulus loops in Fig. 5. The linear stiffness k_1 and k_2 of cross and horizontal strings can be easily calculated. We have used the Newton-Downhill algorithm [37] to solve equations (5).

The Newton-Raphson linearization expression of equations (5) can be written as:

$$\mathbf{u}^{k+1} = \mathbf{u}^{k} + \left(\nabla_{\mathbf{u}}\mathbf{g}^{k}\right)^{-1}\mathbf{g}^{k} \tag{6}$$

Where k denotes the iteration step, and **g**, **u** and $\nabla_{\mathbf{u}}\mathbf{g}$ are expressed as:

$$\mathbf{g}=\begin{bmatrix} g_1 \\ g_2 \\ g_3 \end{bmatrix};\quad \mathbf{u}=\begin{bmatrix} l \\ \theta \\ h \end{bmatrix};\quad \nabla_{\mathbf{u}}\mathbf{g}=\begin{bmatrix} \frac{\partial g_1}{\partial u_1} & \frac{\partial g_1}{\partial u_2} & \frac{\partial g_1}{\partial u_3} \\ \frac{\partial g_2}{\partial u_1} & \frac{\partial g_2}{\partial u_2} & \frac{\partial g_2}{\partial u_3} \\ \frac{\partial g_3}{\partial u_1} & \frac{\partial g_3}{\partial u_2} & \frac{\partial g_3}{\partial u_3} \end{bmatrix} \tag{7}$$

The Newton-Downhill algorithm combines the Newton-Raphson method with the downhill approach:

$$\mathbf{u}^{k+1} = \mathbf{u}^{k} + \lambda\left(\nabla_{\mathbf{u}}\mathbf{g}^{k}\right)^{-1}\mathbf{g}^{k} \tag{8}$$

The downhill factor λ (also called convergence factor) is introduced into the Newton-Raphson expression to guarantee that the vector $\mathbf{u}^{k+1}$ chosen for the next iteration can always get the $\left\|\mathbf{g}^{k+1}\right\| < \left\|\mathbf{g}^{k}\right\|$ condition. The initial value of the downhill parameter is set to 1, and then used to calculate the corresponding $\mathbf{u}^{k+1}$ and $\mathbf{g}^{k+1}$. If $\left\|\mathbf{g}^{k+1}\right\| \geq \left\|\mathbf{g}^{k}\right\|$, λ is halved and $\mathbf{u}^{k+1}$ recalculated until $\left\|\mathbf{g}^{k+1}\right\| < \left\|\mathbf{g}^{k}\right\|$. The parameter λ may therefore assume the values of 1, 1/2, 1/4, 1/8… ε_{λ}, where ε_{λ} is the lower bound forλ.

To assign a suitable $\mathbf{u}^{0}$ value for an efficient use of the Newton-Downhill method to converge, we have used the particle swarm optimization method [38]**.** The objective function for **g** is initially written as:

$$\gamma = g_1^2 + g_2^2 + g_3^2 \tag{9}$$

The theoretical value of the optimized **g** in (9) should be zero. The particle swarm method can only find to make **g** as small as possible. The value of $\mathbf{u}^{0}$ is then assigned to (8), with the following iterations until convergence. The residual ε is set as 0.001 [37].

3. First parametric design and simulation results

The quasi-static deformation simulation of the tensegrity with MR under different external compression forces has been performed and the effect of parameters such as string length ratio, MR stiffness and the initial internal force has been evaluated. Since the diameter of the MR specimen is 20mm, we choose a 20.5mm diameter of the strut. That results in a large and stiff compressive element, with limited distance between struts. The initial parametric design therefore involved the identification of a suitable minimum distance D_{min} (distance between centerlines) to avoid the interference of the struts during compression. Forces in the struts and strings have been also evaluated.

3.1 Size of the structural elements

The effect of the size of the tensegrity elements is evaluated through the string length ratio:

$$\mu = \frac{l_0}{b_0} \tag{10}$$

In (10) l_0 denotes the self-stressed length of the cross string and b_0 refers to the self-stressed length of strut. The material used to build the strut is aluminum and the string is made of steel wire with a diameter of 0.61mm and Young`s modulus of 207GPa.

3.1.1 Variation of the strut length

We started by fixing the external compression force to 200N and the initial inner strut force at 40N. The lengths of the struts and strings have been then varied (Fig. 6). The nearest distance D_{min} initially increases first for increasing values of μ, reaches a peak around$\mu=0.7$ and then sharply decreases. The maximum Dmin increases from 20mm to 40mm as the strut length b_0 increases from 264mm to 448mm. Since the minimum diameter of the strut is 20mm (which should be the same value for D_{min}), the b_0 length used in this paper should be no less than 264mm. The strut force F_b increases nonlinearly with μ, first slowly and then sharply (Fig. 6 (b)). The value of F_b is ~ 190N when$\mu=0.7$. As the strut length increases, the value of F_b does not changes significantly, which indicates the F_b is not sensitive to the variation of the strut length.

From Fig. 6 (c), it can be known that the force in cross string F_s increases almost linearly first with μ, and then starts to rise sharply at the end. The F_s varies from 30N to 60N as the strut length changes from 264mm to 448mm. It shows that the force in cross string is always at low level, although it`s quite sensitive to the strut length. That means the force in cross string is not a key points when designing tensegrity with MR.

It could be seen that the shape and tendency of curves in Fig. 6 (d) is quite similar to those in Fig. 6 (b), which means the force in horizontal strings F_l increases more and more quickly with μ and is not sensitive to strut length. However, F_l is much smaller than F_b, which is around 75N when μ=0.7, compared with 190N of F_b.

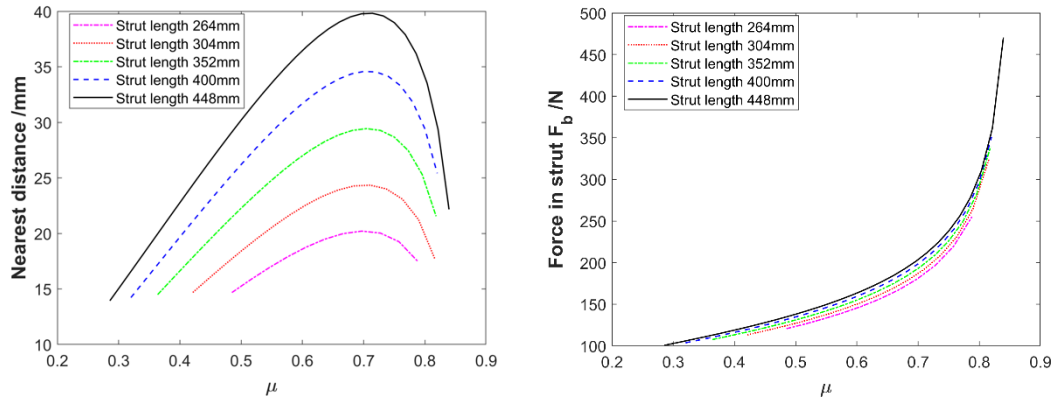

(a) Nearest distance between strut centerline (b) Force in strut

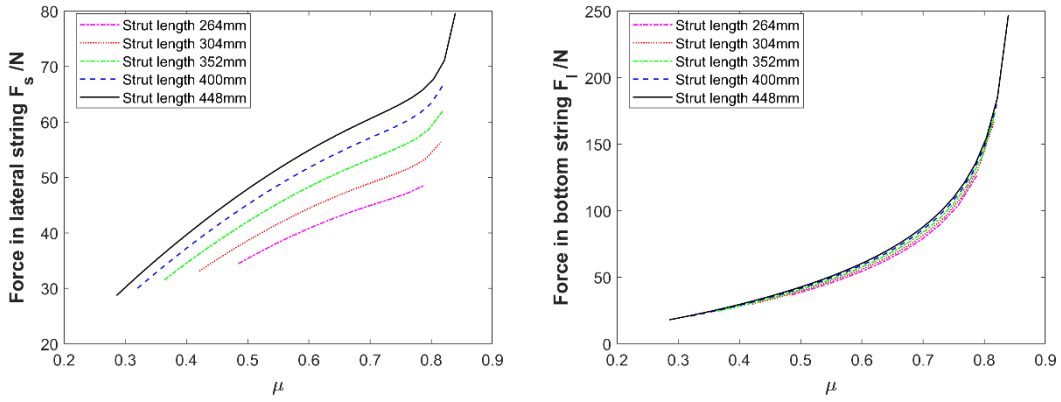

(c) Force in cross string (d) Force in horizontal string

Fig. 6 Comparison between tensegrities with different strut lengths

3.1.2 Variable MR stiffness

Based on the previous simulated results, we set now the strut length b_0 to 350mm and apply an external force of 200N and an initial inner strut force as 40N. We then perform a parametric variation of the MR stiffness from 2 to 3 times the original value to

investigate the sensitivity of the tensegrity system versus the metal rubber mechanical properties (Fig. 7). The figure clearly shows that the stiffness of the MR does not affect significantly the general behavior of the tensegrity configuration. Once the tensegrity becomes stiffer because of the increased metal rubber rigidity, the whole tensegrity configuration becomes more difficult to deform under an external force. The parameter D_{min} therefore increases with the MR stiffness, and all the elements in the tensegrity configuration withstand higher magnitudes of forces.

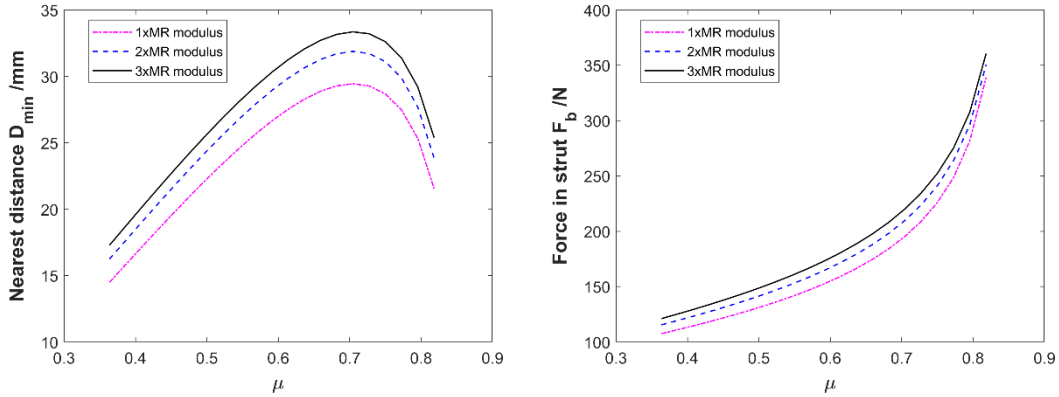

(a) Nearest distance between strut centerline (b) Force in strut

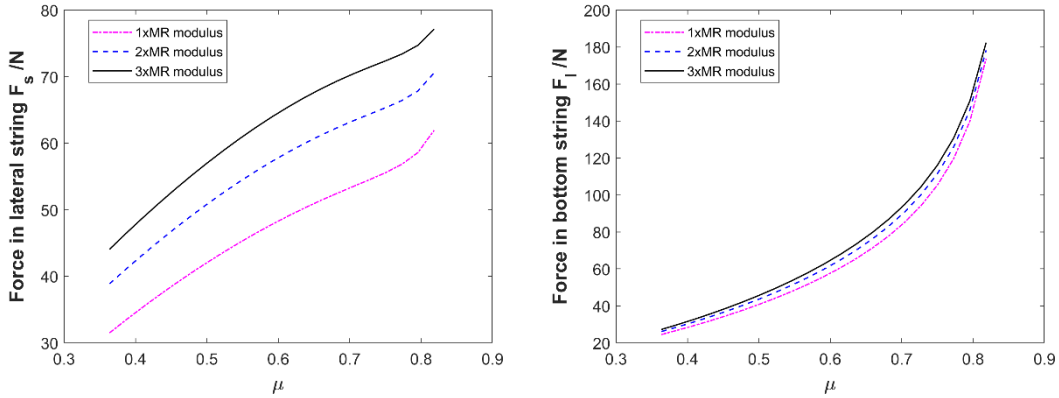

(c) Force in cross string (d) Force in horizontal string

Fig. 7 Comparison between tensegrities with different MR stiffness values

3.1.3 Variable initial inner strut forces

In this particular case we set the reference strut length b_0 to 350mm and apply an external force of 200N. The results can be observed in Fig. 8, and one can notice how the curves are very similar to those shown in Fig. 7. By increasing the pre-compression force the MR will exhibit a higher stiffness (Fig. 5), and the increase of the initial inner

strut force has a similar effect to the increase of MR stiffness. Therefore, both the D_{min} parameter and the different forces increase with the initial inner strut force.

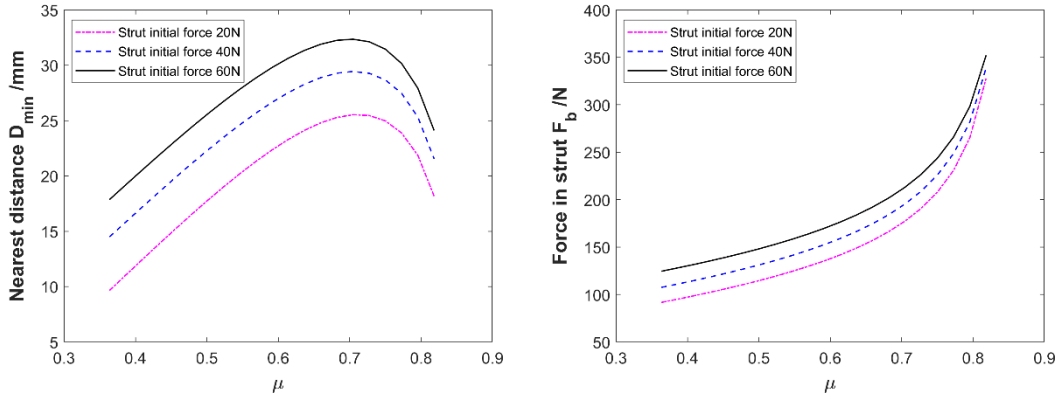

(a) Nearest distance between strut centerline (b) Force in strut

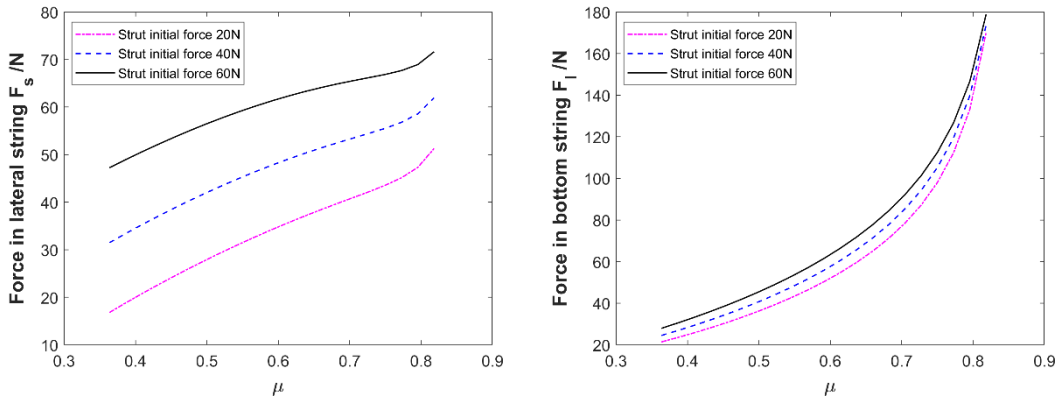

(c) Force in cross string (d) Force in horizontal string

Fig. 8 Comparison between tensegrities with different initial inner strut forces

3.1.4 Variable external compression forces

We set in this case the strut length b_0 to 350mm and apply an initial inner strut force F_{b0} of 40N. The results can be observed in Fig. 8. The variable force F does not affect the overall sensitivity of D_{min} versus μ(Fig. 8(a)). The maximum D_{min} reduces significantly from 42mm to 23mm with the force increasing from 50N to 400N. That indicates that the ideal maximum force F acting on the tensegrity with MR insert should be less than 400N. The variation of F_b and F_l versus μ and F is also quite similar (Fig. 8 (b) and (d)), with an evident increase of F_b and F_l with the force F. Moreover, the forces F_b and F_l tend to be more sensitive to μ when the force F is equal to 400N. This sensitivity is less pronounced when F=50N; that is because the tensegrity has a low aspect ratio of overall dimensions when the parameter μ is large. In this extreme structural condition, the

nonlinear behavior of the tensegrity is more significant than when μ is small. Consequently, the forces F_b and F_l increase significantly with μ when the force F=400N, and change slightly with μ when F=50N.

The curves shown in Fig. 8 (c) are quite interesting. When μ is small (i.e, a slender tensegrity) F_s may decrease with increasing F, which is the opposite of what happens when the parameter μ is large. As μ increases, F_s increases in a more significant way under a larger force F. When F=50N, the strut force F_s is almost constant with changing μ.

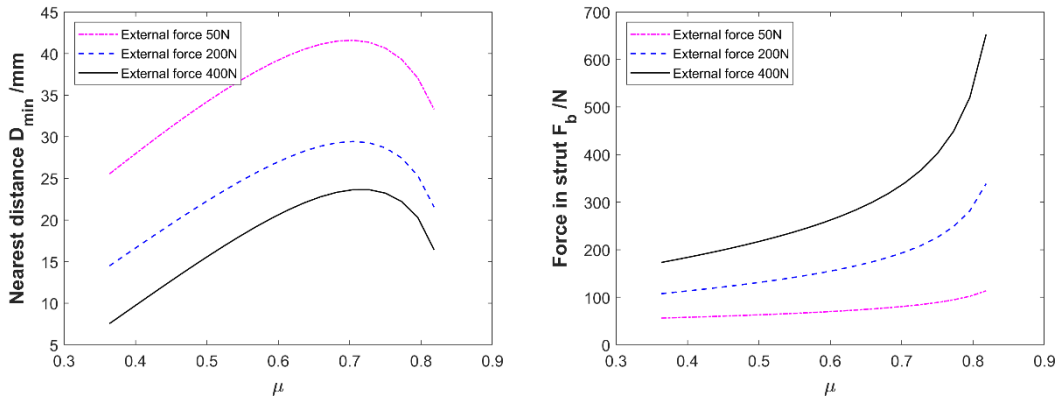

(a) Nearest distance between the strut centerlines (b) Force in the strut

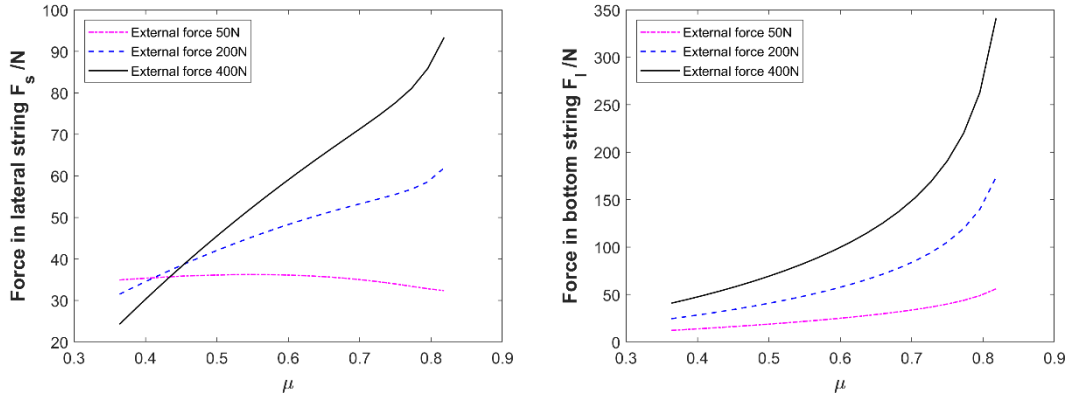

(c) Force in the cross string (d) Force in the horizontal string

Fig. 9 Comparison between tensegrities with different external compression forces

3.2 Nonlinear axial deformation of the tensegrity under an external force

The parametric analysis of the design led us to choose the strut length b_0 of 350mm, and the horizontal string length l_0 of 225mm. The resulting string length ratioμ is 0.64, for which D_{min} is almost maximum and F_b, F_s and F_l are not too large. We then evaluated

the nonlinear behavior of the tensegrity with MR and investigated the effects of parameters like the initial inner strut force F_{b0} and the MR stiffness.

3.2.1 Hysteretic loops of the tensegrity

The initial strut force F_{b0} has been set to 40N, and then used to calculate the cyclic loading and unloading of the tensegrity based on the different loading and unloading MR stiffness shown in Fig. 5. It is possible in this way to simulate the hysteretic cycles under different maximum external compression forces, as shown in Fig. 10.

The loading curve has a displacement hardening behavior caused both by the nonlinearity of the metal rubber and the nonlinear geometric deformation of the tensegrity. It should be however noticed that the nonlinearity is not severe. The loss factors of the tensegrity under different maximum external forces can be calculated from Fig. 10 [36], and the result is shown in Table. 4 The loss factor increases significantly with the force, from 0.045 when F=50N to 0.097 when F=400N. This is opposite of what observed with the MR alone (Table. 3), with the material loss factor reducing slightly with increasing F (from 0.173 for F=100N to 0.151 when F=450N). The loss factor of the tensegrity configuration is in general significantly smaller than the one of the MR. The discrepancy between the loss factor behaviors can be explained by considering the different forces acting on the MR inserts and the tensegrity system. The force applied on the MR specimen, which is same as the force exerted in the strut of the tensegrity, is used to calculate the loss factor of the MR insert. On the opposite, the force applied on the top end of the tensegrity should be the one to be used for the calculation of the loss factor of the whole tensegrity. This force is very different from the one present in the strut.

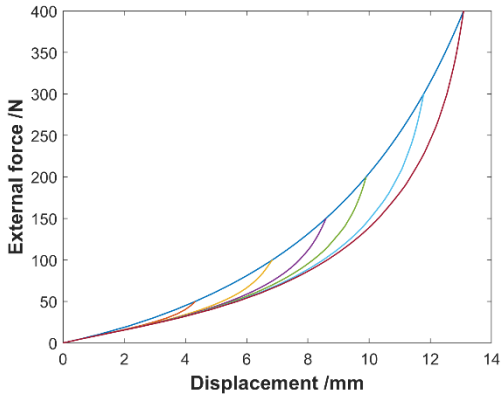

Fig. 10 Hysteretic loops of the tensegrity prism with MR

Table. 4 Loss factors of tensegrity under different maximum F

Maximum F	50N	100N	150N	200N	300N	400N
Loss factor	0.045	0.065	0.076	0.086	0.093	0.097

The simulated hysteretic loops of the MR assembled inside the tensegrity and obtained from the simulations of the nonlinear behavior of the tensegrity are shown in Fig. 11. One can observe a strong similarity of these results with the experimental ones (Fig. 4 (c)); this feature indicates in one aspect that the tensegrity model proposed is reliable.

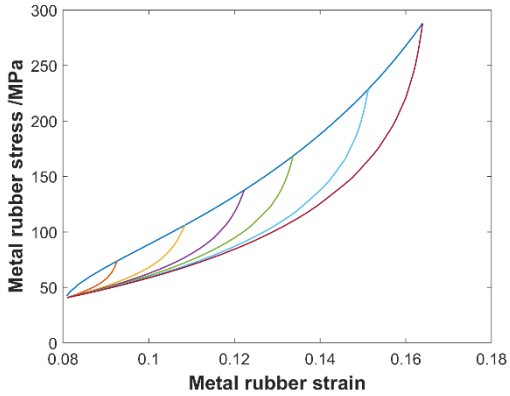

Fig. 11 Hysteretic loops of the MR specimen inside the tensegrity prism

3.2.2 Effect of the initial internal force

When we vary the force Fb0 from 20N, 40N and 60N and then perform the compression simulation and benchmark the curve results, shown in Fig. 12 and Fig. 13. The tensegrity becomes stiffer for the largest values of F_{b0} because the stiffness of the MR inserts becomes higher when the pre-compression force increases (Fig. 3), and

consequently the stiffness of tensegrity increases. Apart from the specific values of their magnitude, the shapes of the force-displacement curves are similar for the various values of F_{b0}.

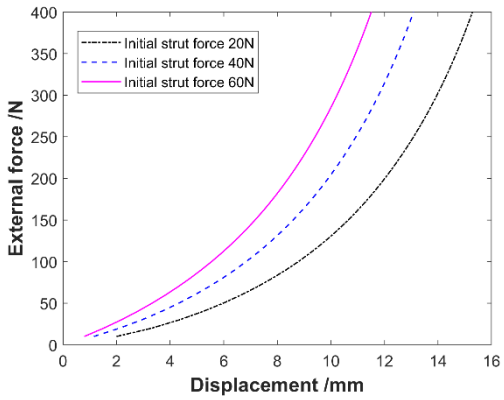

Fig. 12 Force-displacement curves of the tensegrity prism with different F_{b0} values

The results related to D_{min}, F_b, F_s and F_l are shown in Fig. 13. The diameter D_{min} reduces nonlinearly with increasing values of F, with a fast decreasing rate for low values of the load and a significantly slower decreasing rate at high force levels. In order to keep the D_{min} parameter greater than 25mm, one should choose $F_{b0} \geq 40N$ and $F \leq 250N$. Moreover, D_{min} increases with larger values of F_{b0}, as the tensegrity becomes stiffer. From Fig. 13 (b)-(d) it can be also observed that the internal tensegrity F_b, F_s and F_l increase almost linearly with F, especially when F_{b0} is large. The maximum forces in the different strings are close to 120N when F is equal to 400N; this force is not very large for the steel wire used to assemble the tensegrity. The maximum force Fb is close to 300N when F=400N, which is acceptable for MR samples [36]. It is also possible to notice that the forces F_b, F_s and F_l increase almost linearly with F_{b0}.

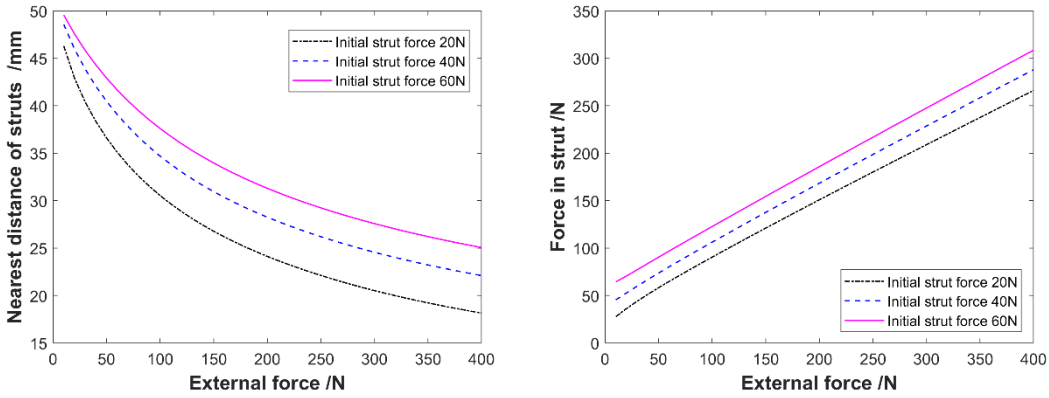

(a) Nearest distance between strut centerline (b) Force in strut

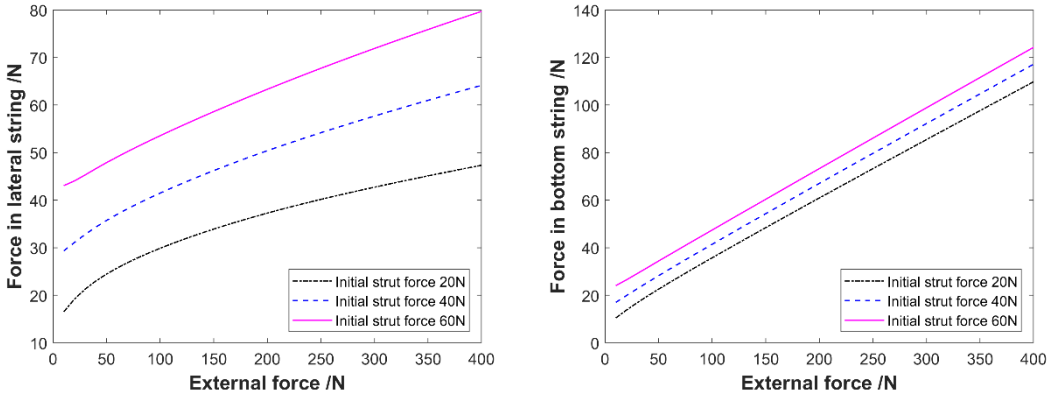

(c) Force in the cross string (d) Force in the horizontal string

Fig. 13 Comparison between tensegrities with different initial inner strut forces

3.2.3 Effect of the MR stiffness

For F_{b0} equal to 40N and for MR stiffness increases from 2 to 3 times the nominal value, one can obtain the behavior of the tensegrity configurations shown in Fig. 14. As observed and discussed above, the effect of MR stiffness is quite similar to the one provided by the force F_{b0}, both in terms of results and general sensitivity. The results of Fig. 14 are therefore quite similar to the ones illustrated in Fig. 12, in which the tensegrity becomes stiffer with higher MR stiffness values and the nonlinearity behavior is quite similar. The curves related to the variation of D_{min}, F_b, F_s and F_l for the different MR stiffnesses are omitted here because of the similarity with the graphs shown in Fig. 13.

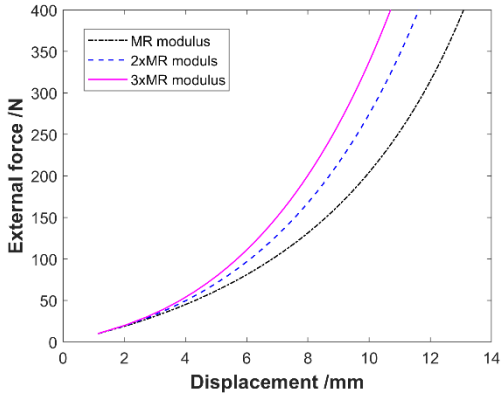

Fig. 14 Force-displacement curves of the tensegrity prism with different MR stiffness values

4. Tensegrity structure design and assembly

Based on the results of the parametric simulations we finally chose a strut length b_0 of 350mm and an horizontal string length l_0 of 225mm. Since the diameter of the MR specimen is 20mm the diameter of the strut should not be lower than 20mm (final value: 20.5mm). We have used aluminum to build the strut and reduce the weight. The strings consist of piano string steel wires with a nominal diameter of 0.61mm, Young`s modulus of 207GPa and tensile strength of 1586MPa. The design of the 3D model of the tensegrity with MR is shown in Fig. 15. We have added two triangle plates at the top and bottom to apply the loading in quasi-static compressive, vibration and impact tests.

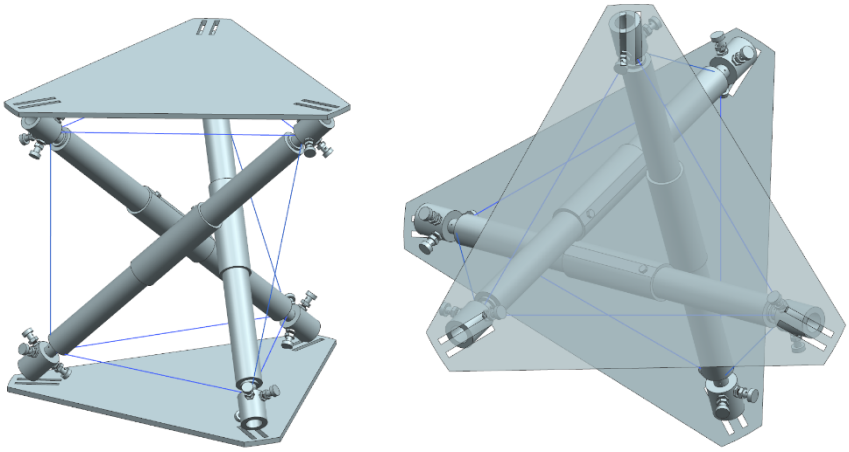

Fig. 15 3D model of the tensegrity with MR (left isometric, and right top views)

The detailed design of strut with the metal rubber insert is illustrated in Fig. 16. Two separate aluminum bars are used to assemble the strut, with the MR specimen in the middle attached to both bars with metal glue. The metal rubber is surrounded by the aluminum sleeve, which fits within the aluminum bars with a small tolerance. The function of the aluminum sleeve is to enhance significantly the buckling stress of the strut, while at the same time permitting the MR to deform normally. With the sleeve the aluminum bar could also slide in an easier way.

At each end of the strut a steel joint is attached by a screw. The reason behind the choice of steel to make the joint is about the requirement to add three bolts at each joint, which would need to be frequently adjusted. Compared to a steel case, a screw made of aluminum would easily wore out. Three small holes are drilled at the neck of the steel

joint (Fig. 16). The steel wire is inserted through the hole and then fixed by the adjusting bolt. By turning the adjusting bolt, the length of the string could be changed, thus the pre-tension force in the string can be modified. The locking nut is added to block the string tension. A hole is drilled at the end of the steel joint to connect the same joint to the plate by binding with steel wire.

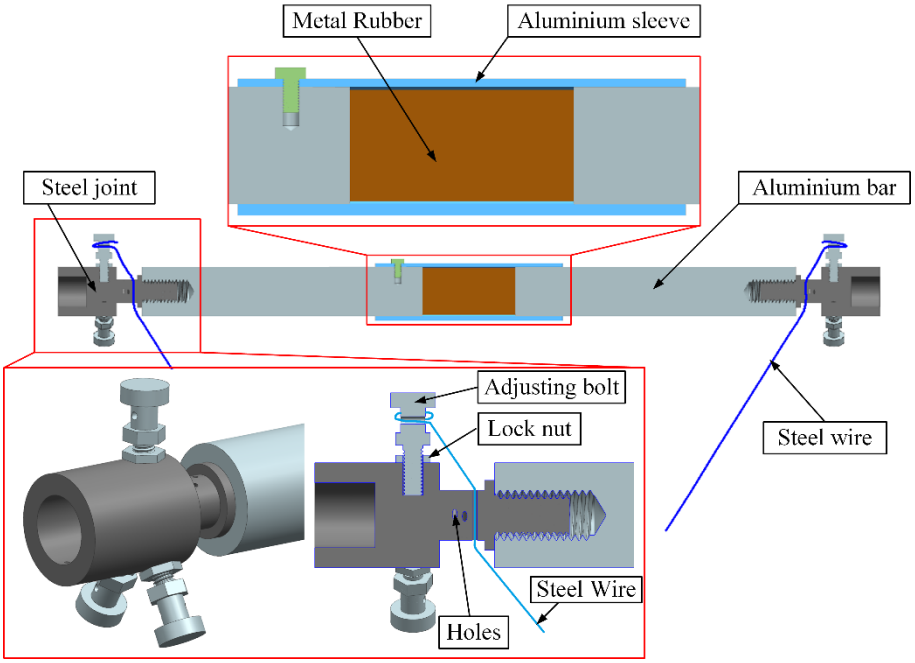

Fig. 16 Illustration of struts with MR in tensegrity

Two tensegrity samples have been built, one with the metal rubber and other without (Fig. 17). The configuration and size of the two tensegrity systems are the same, except for the internal structure of the strut, with a pure aluminum bar replacing the complex system of Fig. 16 for the case of the 'pristine' tensegrity. The most complicated procedure during the assembly of the tensegrity is the adjustment of the pre-tension force in the strings. Due to the difficulty of measuring the pre-tension force directly, we have used a microphone to measure the frequency of the sound generated by the string and then calculated the pre-tension force based on the resonance vibration [39]:

$$f = \frac{n}{2l}\sqrt{\frac{T}{\rho A}} \tag{11}$$

where n denotes the index of the mode, l is the length of the string, T denotes the pre-tension force, ρ is the density of the steel wire and A is the cross-section of the string.

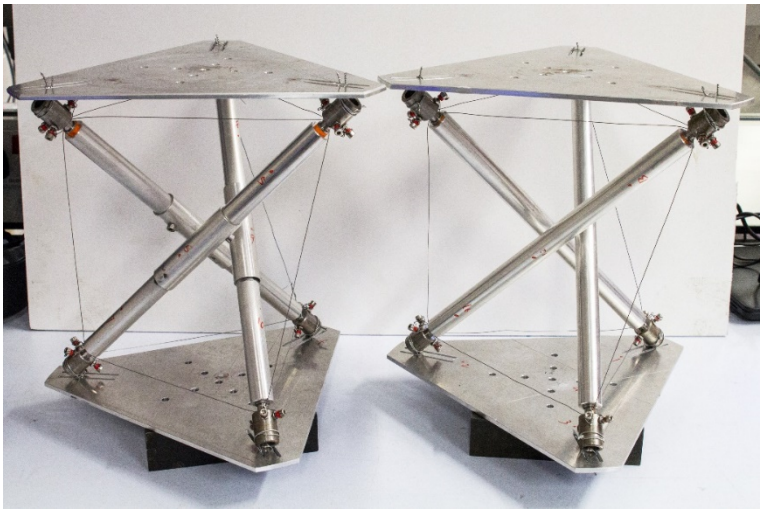

Fig. 17 Tensegrity prototypes

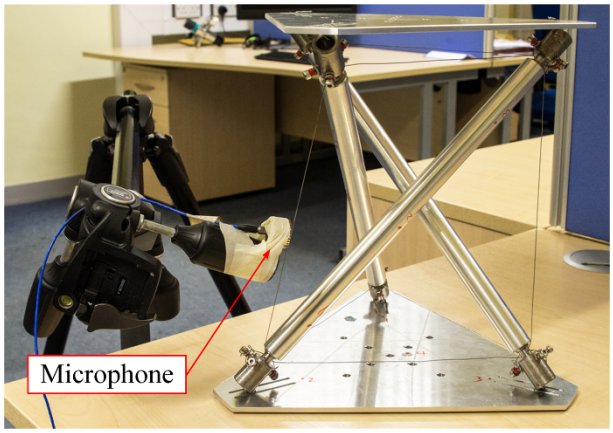

Fig. 18 Measuring the pre-tension of strings

5. Quasi-static tests results and discussions

The quasi-static tests were performed by a SHIMADZU machine under force control, with the loading and unloading rate at 1N/s. The test rig is shown in Fig. 19. Because the tensegrity prism rotates under a compression load [35,40], a thrust bearing was added between the compression plate of the machine and the upper plate of the tensegrity to reduce the friction between the two plates caused by the twist during the test.

The first couple of hysteresis loops of the tensegrity are dissimilar from the following ones because of the unstable initial state of MR and the slack within the tensegrity joints, as also discussed in section 2 and reference [36]. The first three hysteresis loops at the

beginning of the test are therefore ignored, and the results are recorded from the 4th loop onwards. Each hysteretic cycle from the different tensegrities at different loading conditions was tested for three times and averaged.

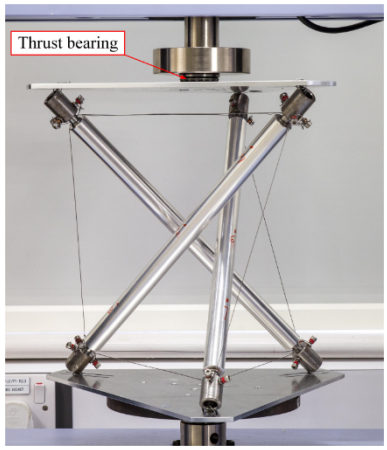

Fig. 19 Quasi-static test rig of tensegrity

The results from the two classes of tensegrity are shown in Fig. 20. The maximum loading forces in the different hysteresis loops are 50N, 100N and 150N. The loading curves with different maximum forces coincide well with each other. It is also evident that the stiffness of the tensegrity without MR is significantly larger than the one of the tensegrity with MR.

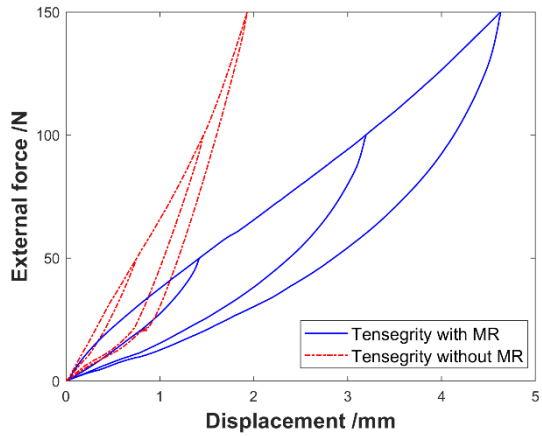

Fig. 20 Experimental force vs displacement curves of the different tensegrity prisms

The comparison between simulated and tested quasi-static compression results of tensegrity with and without MR are shown in Fig. 21 and Table. 5. The experimental stiffness is significantly larger than the one obtained from the simulations. The variation between the experimental and the simulated tangent stiffness of the tensegrity without

MR is also significantly higher than the one of the tensegrity with MR (Fig. 21 (b)). It should also be noticed than the experimental tangent stiffness of the two tensegrity configurations first decreases, and then increases with the deformation. On the contrary, the tangent stiffness from the simulation tends to become larger with increasing deformations. The experimental loss factor is also greater than the simulated one (Table. 5). The tested loss factor of tensegrity without MR is quite big while the simulated loss factor is 0. It should also be noticed that the loss factor of both tested and simulated result increase obviously with maximum loading force.

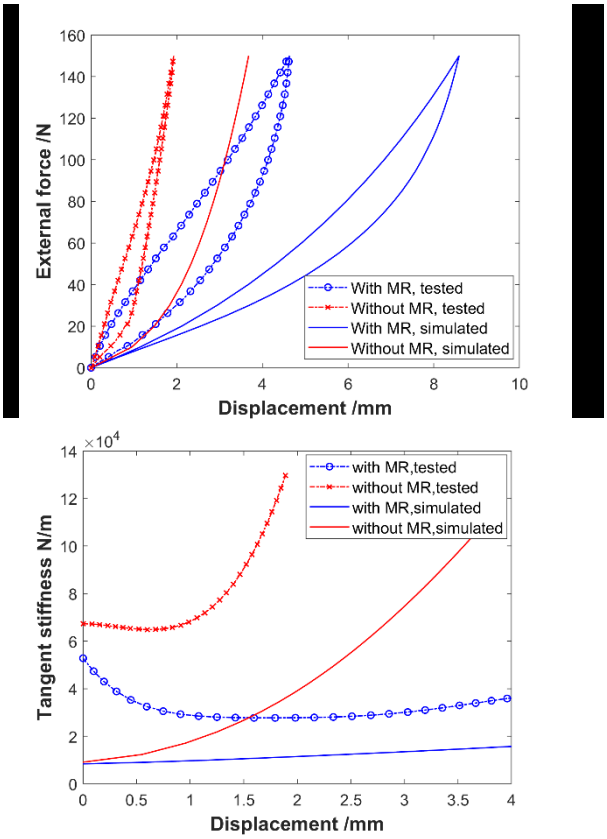

(a) Force vs displacement curves (b) Tangent stiffness vs displacement curves

Fig. 21 Comparison between simulations and tests of the tensegrities with and without MR

Table. 5 Loss Factors related to the simulated and experimental results

Maximum force /N	Experiments		Simulations	
	with MR	without MR	with MR	without MR
50	0.110	0.068	0.045	0

100	0.157	0.128	0.065	0
150	0.164	0.127	0.076	0

6. New tensegrity MR model

The deviation between the simulated and experimental results may be caused by the following reasons:

(1) The top and bottom strings of the built tensegrity prisms are constrained by the plates and cannot deform freely. The top and bottom strings should therefore be considered as rigid compared with the cross strings.

(2) The joints between plates and struts are not ideal pin joints, and that may introduce localized stiffness and friction and affect the results.

(3) The stiffness and damping of the struts with MR may be slightly different from the ones of the MR specimens because of the friction between sleeves and bars. The simulations have been however carried out using the mechanical properties of the MR specimens for the struts, and this may have provided further discrepancies with the experimental results.

6.1 Comparison between MR specimens and struts with MR

In order to check the effect of the friction between sleeves and bars of the struts with the MR inserts we have tested the 3 struts with MR, and compared the results with the ones from the pure MR specimens. The quasi-static test was conducted using a SHIMADZU machine (Fig. 22). The test was conducted by force control, with the loading rate and unloading rate both to be 1N/s (similar to the test conducted on the MR specimens). The first three hysteresis loops at the beginning of the test are discarded, and the results are recorded from the 4^{th} loop onwards.

Fig. 22 Quasi-static test of struts with MR

The difference between struts and pure MR specimens does not appear as significant as the one observed between the simulated and experimental data of the whole tensegrities (Fig. 23 and Table. 6). The hysteretic loops of the three struts also tend to be all similar. One could therefore average the results from the three struts and the three specimens to obtain the secant modulus and the loss factor of the strut with the MR, and the MR tensegrity specimen. The discrepancy between struts and MR specimens is less than 25%, and the sensitivity versus the compressive strains is also similar. The secant modulus and the loss factor of the struts are larger than the one observed in the MR specimen, and this is due to the friction between sleeve and bar in the strut with the metal rubber. We can therefore conclude that the difference between the mechanical performance of the struts and the pure MR specimens is not the main factor justifying the presence of the observed deviation between the experimental and simulated results of the tensegrity assembly.

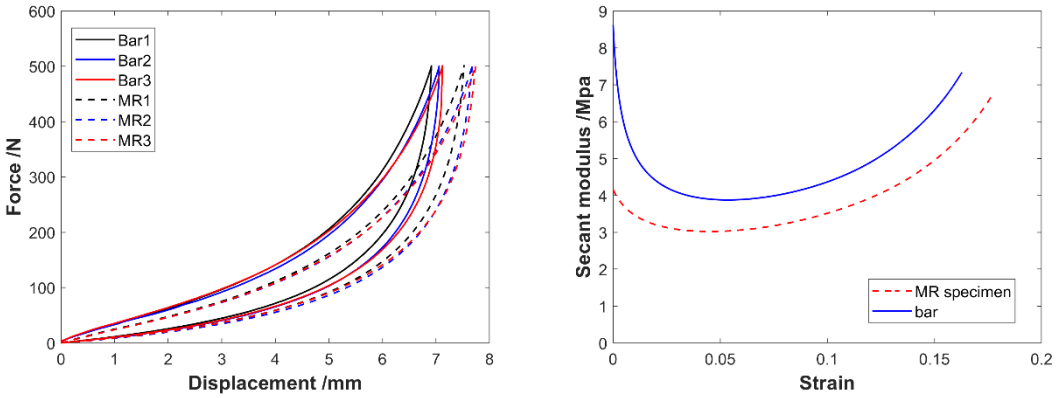

(a) Hysteretic loops (b) Secant modulus

Fig. 23 Test result comparison between struts with MR and MR specimens

Table. 6 Loss factors of struts with MR and MR specimens

Pre-compression Force	MR specimen	Strut
0N	0.145	0.176
20N	0.130	0.161
40N	0.116	0.145
60N	0.105	0.132

6.2 New theoretical model of the tensegrity

The tensegrity original theoretical model has been modified based on the above cited three conditions (Paragraph 6, Fig. 24). An angular spring is added to each joint, while a friction element that can totally describe the friction introduced by the presence of joints, sleeves and the test rig compression plate is added to the whole tensegrity prism. The modulus of the top and bottom strings is numerically set at 10000 GPa compared to the 210GPa of the cross strings, i.e. the top and bottom strings can be considered as rigid bodies.

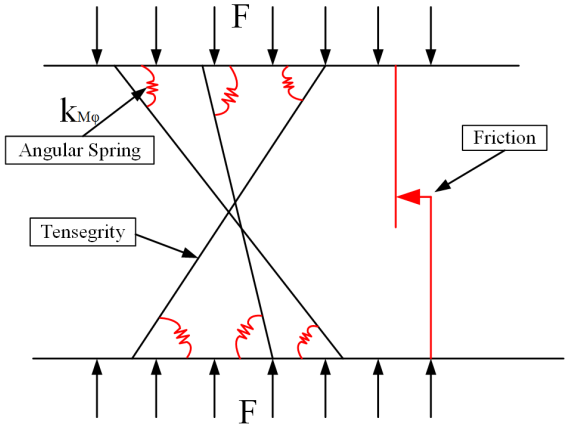

Fig. 24 Illustration of calibrated tensegrity theoretical model

The moment introduced by the angular spring is expressed as follows:

$$M_{\varphi} = F_M b = k_{M\varphi}\left(\varphi_h - \varphi_{h0}\right) \tag{12}$$

In (12) M_{φ} is the moment caused by the angular spring, F_M is the equilibrium force generated at the joints by the moment, b is the length of the strut, $k_{M\varphi}$ is the torsional stiffness, φ_h is the spatial angle between the strut and plate, and φ_{h0} is the spatial angle between the strut and the plate at the initial state of the tensegrity. The spatial angle φ_h can be obtained as:

$$\varphi_h = \arcsin\left(\frac{h}{b}\right) \tag{13}$$

In (12) h is the height of the tensegrity. The equilibrium force F_M can be decomposed along the x, y, z Cartesian axes as follows:

$$\begin{aligned} F_{Mx} &= F_M \sin\varphi_h \sin\theta \\ F_{My} &= F_M \sin\varphi_h \cos\theta \\ F_{Mz} &= F_M \cos\varphi_h \end{aligned} \tag{14}$$

Where θ is the twisting angle of tensegrity (Fig. 1). By imposing the equilibrium of the moments around the 3 Cartesian directions, and the friction force into the equilibrium equations in (3) one can obtain the new equilibrium equations of the tensegrity theoretical model:

$$
\begin{aligned}
g_1 = 0 &= \frac{1}{6} l \left[2\sqrt{3}\left(x_1 + 3x_2 - x_3\right) + \sqrt{3}\left(x_1 + 2x_3\right)\cos\theta - 3x_1 \sin\theta \right] - F_{Mx} \\
g_2 = 0 &= \frac{1}{6} l \left[\sqrt{3}\left(x_1 + 2x_3\right)\sin\theta + 3x_1 \cos\theta \right] + F_{My} \\
g_3 = 0 &= h\left(x_3 - x_1\right) - \frac{F}{3} + F_{Mz} + \frac{F_f}{3}
\end{aligned}
\tag{15}
$$

In (15) F_f is the friction force, which is different during loading and unloading (it is F_{fl} during loading, and F_{fu} in the unloading phase). In classic friction models the friction force should be expressed as the function of the relative displacement between the two mating surfaces [41,42]. However, in this model, the friction element represents the combined friction in the joints, sleeves and compression plates. Consequently, the friction force shown in Fig. 24 is a function of the compression force *F*:

$$
\begin{aligned}
F_{fl}\left(F\right) &= \begin{cases} \alpha F & \left(F \le F_1\right) \\ \alpha F_1 + \beta\left(F - F_1\right) & \left(F > F_1\right) \end{cases} \\
F_{fu}\left(F\right) &= \begin{cases} \beta F & \left(F \le F_2\right) \\ \beta F_2 + \alpha\left(F - F_2\right) & \left(F > F_2\right) \end{cases}
\end{aligned}
\tag{16}
$$

The friction forces during loading and unloading are expressed as piecewise functions, and the corresponding hysteric loop is shown in Fig. 25. During loading the contact model is considered in stick condition when $F \le F_1$, and the friction force is linear with a stick friction coefficient α. When $F > F_1$ the contact element is in sliding condition. In normal contact models, the friction force is constant during slide ($F_{fslide} = \mu N$, where μ represents the coefficient of sliding friction and *N* represents the normal contact force). In the tensegrity the normal contact *N* force increases with the external loading force *F*. That increase implies that the sliding friction force should also increase, even though the contact model enters slide. We therefore suppose that the sliding friction force is linear to the external force *F*, with a sliding friction coefficient β.

During unloading the displacement of the tensegrity prism starts to decrease from the

maximum loading position and the contact element is in stick when $F > F_2$. On the contrary, when $F \le F_2$ the contact enters slide. The stick and slide friction coefficients α and β during unloading should be the same as the ones during loading, with $\alpha > \beta$.

In order to obtain an enclosed hysteretic loop of friction as shown in Fig. 25, the equivalent relation should hold:

$$F_{fl}\left(F_0\right) = F_{fu}\left(F_0\right) \tag{17}$$

In (17) F_0 is the maximum loading force. By substituting (16) into (17) we then obtain the following equation:

$$F_0 = F_1 + F_2 \tag{18}$$

The three unknown parameters α, β and F_1 are sufficient to describe the friction element in Fig. 24. However, the piecewise function of the friction model in equation (16) is not derivable. When substituted into equations (15) the resulting **g** function will also become non-derivable, making therefore the Newton-Downhill algorithm (7) to fail. To overcome this problem we have used a sigmoid function to describe the friction by multiplying by a parameter *a*:

$$S\left(x\right) = \frac{1}{1+e^{-ax}} \tag{19}$$

The parameter has been set as $a = 0.2$ to smooth the turning points between the stick and slide conditions. Substituting the sigmoid function (19) into the piecewise friction equations (16), the new friction model can then be rewritten into a derivable form:

$$\begin{aligned} F_{fl}\left(F\right) &= \left[1 - \frac{1}{1+e^{-0.2\left(F-F_1\right)}}\right]\alpha F + \frac{1}{1+e^{-0.2\left(F-F_1\right)}}\left[\alpha F_1 + \beta\left(F - F_1\right)\right] \\ F_{fu}\left(F\right) &= \left[1 - \frac{1}{1+e^{-0.2\left(F-F_0+F_1\right)}}\right]\beta F + \frac{1}{1+e^{-0.2\left(F-F_0+F_1\right)}}\left[\beta\left(F_0 - F_1\right) + \alpha\left(F - F_0 + F_1\right)\right] \end{aligned} \tag{20}$$

The comparison between the piecewise and derivable friction function curves is shown in Fig. 25 ($\alpha = 0.7$, $\beta = 0.3$, $F_1 = 40$, $F_0 = 150$ and $a = 0.2$).

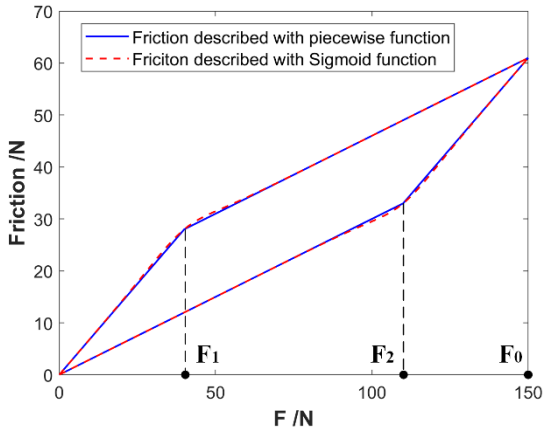

Fig. 25 Comparison between the curves of the two different friction functions

Finally, when substituting the corresponding equations into (15) we obtain the final equilibrium equations of the tensegrity theoretical model:

$$
\begin{aligned}
g_1 = 0 = \frac{l}{6}\Bigg[& 4k_3 \sin^2\left(\frac{\theta}{2}\right)\left(\sqrt{3} - \frac{3b_N}{\sqrt{3h^2 - 2l^2\cos\theta + 2l^2}}\right) + k_1\left(-3\sin\theta + \sqrt{3}\cos\theta + 2\sqrt{3}\right) + k_2\frac{6\sqrt{3}\left(l - l_N\right)}{l} - k_1\frac{3s_N\left(-\sqrt{3}\sin\theta + \cos\theta + 2\right)}{\sqrt{3h^2 - \sqrt{3}l^2\sin\theta + l^2\cos\theta + 2l^2}}\Bigg] \\
& - \frac{k_{M\varphi}h\sin\theta}{h^2 - \frac{2}{3}l^2\cos\theta + \frac{2}{3}l^2}\left(\varphi_{h0} - \varphi_h\right) \\
g_2 = 0 = \frac{l}{6}\Bigg[& 2k_3\sin\theta\left(\frac{3b_N}{\sqrt{3h^2 - 2l^2\cos\theta + 2l^2}} - \sqrt{3}\right) + k_1\left(\sqrt{3}\sin\theta + 3\cos\theta\right) - k_1\frac{3s_N\left(\sin\theta + \sqrt{3}\cos\theta\right)}{\sqrt{3h^2 - \sqrt{3}l^2\sin\theta + l^2\cos\theta + 2l^2}}\Bigg] \\
& + \frac{k_{M\varphi}h\cos\theta}{h^2 - \frac{2}{3}l^2\cos\theta + \frac{2}{3}l^2}\left(\varphi_{h0} - \varphi_h\right) \\
g_3 = 0 = & -\frac{F}{3} + k_3 h\left(\frac{b_N}{\sqrt{h^2 - \frac{2}{3}l^2\cos\theta + \frac{2l^2}{3}}} - 1\right) + k_1 h\left(\frac{\sqrt{3}s_N}{\sqrt{3h^2 - \sqrt{3}l^2\sin\theta + l^2\cos\theta + 2l^2}} - 1\right) + \frac{k_{M\varphi}\sqrt{-\frac{2}{3}l^2\cos\theta + \frac{2}{3}l^2}}{h^2 - \frac{2}{3}l^2\cos\theta + \frac{2}{3}l^2}\left(\varphi_{h0} - \varphi_h\right) + \frac{F_f}{3}
\end{aligned}
\tag{21}
$$

In (21) F_f indicates the different loading and unloading forces (equation (20)). The remaining 4 unknown parameters $k_{M\varphi}$, α, β and F_1 in (21) are determined from the tests. We have used the particle swarm method to for the identification with parallel computing to speed up the optimization process. Seven locations in the force vs. displacement curve have been used (Fig. 26), corresponding to F=25N, 50N, 100N and 150N. The objective function of the optimization was:

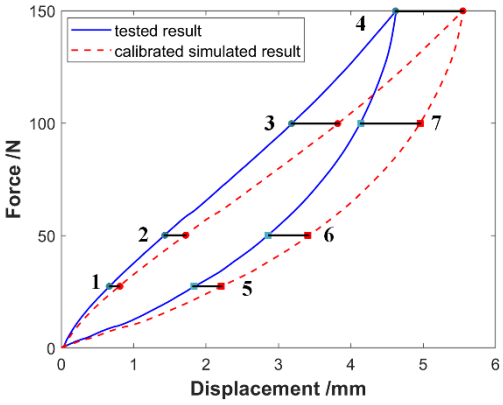

Fig. 26 Illustration of optimization points

$$p\left(k_{M\varphi},\alpha,\beta,F_1\right)=\sum_{n=1}^{7}\left(x\left(F_n\right)-x_n\right)^2+q\left(\alpha,\beta\right) \tag{22}$$

$$q\left(\alpha,\beta\right)=\begin{cases}0 & \left(\alpha>\beta\right)\\ 10^7 & \left(\alpha\le\beta\right)\end{cases} \tag{23}$$

In equation (22) $x\left(F_n\right)$ refers to the displacement calculated by the model when $F=F_n$. The experimental displacement is x_n, while $F=F_n$. $q\left(\alpha,\beta\right)$ is the weight used to fulfill the constraint $\alpha>\beta$ (equation (23)).

6.3 Results of the calibrated theoretical model

The optimized coefficients of the model are shown in Table. 7. The parameters associated to the friction element in the models with and without MR are quite similar, while the torsional stiffness differs significantly. The torsional stiffness in the pristine tensegrity is larger than in the case with metal rubber; a likely explanation is because the deformation of the pristine tensegrity is much smaller and the joints mainly remain in stick condition during the test. On the contrary, the deformation of the tensegrity with MR is significantly higher, and the joints would enter the sliding state during the deformation. The torsional stiffness of the tensegrity without MR is also larger because no bilinearity of the torsional stiffness has been considered. It is also worth of notice that the value of the optimized objective function of the tensegrity without MR is smaller than the case with metal rubber.

Table. 7 Results from the optimization calculations

Parameters	$k_{M\varphi}$ (N.mm)	α	β	F_1 (N)	Optimized objective function value	Loss factor	
						Tested	model
Tensegrity without MR	53394	0.7466	0.5	60	0.046	0.127	0.129
Tensegrity with MR	10000	0.7216	0.5	60	0.149	0.164	0.155

The comparison between the calibrated and tested results is shown in Fig. 27. The hysteretic loops of the calibrated model and the experiments agree with each other quite well, especially during loading (Fig. 27(a). The comparison of the tangent stiffness during loading is shown in Fig. 27(b), and the overall trend and averaged values of the tangent stiffness curves have again a good agreement, although with a noticeable deviation at small deformations. The comparison between the loss factors is shown in Table. 7, and the deviation between model and experimental values is lower than 6%.

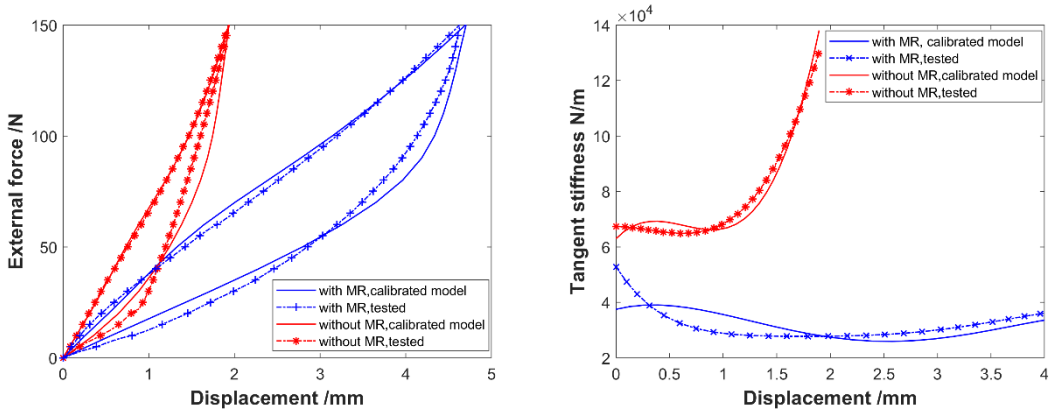

(a) Force vs displacement curve (b) Tangent stiffness vs displacement curve

Fig. 27 Comparison between the calibrated and the tested results related to the tensegrities with and without MR

7. Conclusions

The pristine prism and the metatensegrity concept described in this work show that the damping capacity of the tensegrity increases significantly while the axial stiffness is significantly reduced after the use of metal rubber inserts inside the struts. The significant improvement of energy dissipation can be used in applications where tensegrity prisms are used in vibration and impact working conditions, like a tensegrity-based deployable robot probe for planetary exploration [6]. It also worth noticing that

a smooth and derivable friction model was here developed to enhance the baseline tensegrity model, and provides good agreement with a classical normal bilinear model. This model could also be used in conditions when a derivation is needed for the friction force to function.

Acknowledgement

FS and RES thank the UK Royal Society grant IE161769 for the funding of the International Collaboration Scheme between Bristol and Texas A&M. QZ and DZ acknowledge the National Natural Science Foundation of China (Grant numbers: 51475021 and 11672017) and the China Scholarship Council for the financial support during their stay in Bristol.

Reference

[1] Motro R. Tensegrity Systems: The State of the Art. Int J Space Struct. 1992;7(2):575-582.
[2] Snelson K. Continuous tension, discontinuous compression structures. United States patent 3169611, Feburary, 1965.
[3] Pugh A. An Introduction to Tensegrity. University of California Press, 1976.
[4] Skelton R E, Oliveira M C D. Tensegrity Systems. Springer, Berlin, 2011.
[5] Skelton R E, Montuori R, Pecoraro V. Globally stable minimal mass compressive tensegrity structures. Compos Struct 2016;141:346-354.
[6] SunSpiral V, Gorospe G, Bruce J, Iscen A, Korbel G, Milam S, et al. Tensegrity based probes for planetary exploration: Entry, descent and landing (EDL) and surface mobility analysis. International Journal of Planetary Probes 2013;7.
[7] Fabbrocino F, Carpentieri G. Three-dimensional modeling of the wave dynamics of tensegrity lattices. Compos Struct 2017;173:9-16.
[8] Fraternali F, Senatore L, Daraio C. Solitary waves on tensegrity lattices. J Mech Phys Solids 2012;60(6):1137-1144.
[9] Fraternali F, Carpentieri G, Modano M, Fabbrocino F, Skelton R E. A tensegrity approach to the optimal reinforcement of masonry domes and vaults through fiber-reinforced composite materials. Compos Struct 2015;134:247-254.
[10] Tibert A G, Pellegrino S. Deployable tensegrity reflectors for small satellites. J Spacecr Rockets 2002;39(5):701-709.
[11] Zolesi V S, Ganga P L, Scolamiero L, Micheletti A, Podioguidugli P, Tibert G, et al. On an innovative deployment concept for large space structures. 42nd International Conference on Environmental Systems 2012;3601.
[12] You Z, Pellegrino S. Cable-stiffened pantographic deployable structures. I-Triangular mast. AIAA J 1996;34(4):813-820.
[13] Khazanov M, Jocque J, Rieffel J. Evolution of locomotion on a physical tensegrity robot. ALIFE 2014;14:232-238.
[14] Koizumi Y, Shibata M, Hirai S. Rolling tensegrity driven by pneumatic soft actuators. IEEE International Conference on Robotics and Automation 2012;1988-1993.
[15] Shibata M, Saijyo F, Hirai S. Crawling by body deformation of tensegrity structure robots. IEEE International Conference on Robotics and Automation 2009;3617-3622.
[16] Zhang Q, Zhang D, Dobah Y, Scarpa F, Fraternali F, Skelton R E. Tensegrity cell mechanical metamaterial with metal rubber. Appl Phys Lett 2018;07
[17] Ma Y, Zhang Q, Zhang D, Scarpa F, Gao D, Hong J. Size-dependent mechanical behavior and boundary layer effects in entangled metallic wire material systems. J Mater Sci 2017;52(7):3741-3756.
[18] Ertas B, Al-Khateeb E, Vance J. Cryogenic temperature effects on metal mesh dampers and

liquid hydrogen turbopump rotordynamics. 38th AIAA/ASME/SAE/ASEE Joint Propulsion Conference & Exhibit 2002;4164.
[19] Zarzour M, Vance J. Experimental evaluation of a metal mesh bearing damper. J Eng Gas Turbines Power-Trans ASME 2000;122(2):326-329.
[20] Ma Y, Zhang Q, Zhang D, Scarpa F, Liu B, Hong J. Tuning the vibration of a rotor with shape memory alloy metal rubber supports. J Sound Vibr 2015;351:1-16.
[21] Ma Y, Zhang Q, Zhang D, Scarpa F, Liu B, Hong J. The mechanics of shape memory alloy metal rubber. Acta Mater 2015;96:89-100.
[22] Zhang D, Scarpa F, Ma Y, Hong J, Mahadik Y. Dynamic mechanical behavior of nickel-based superalloy metal rubber. Mater Des 2014;56(4):69-77.
[23] Ma Y, Zhang Q, Zhang D, Scarpa F, Liu B, Hong J. A novel smart rotor support with shape memory alloy metal rubber for high temperatures and variable amplitude vibrations. Smart Mater Struct 2014;23(12):125016.
[24] Ma Y, Zhang Q, Zhang D, Hu W, Hong J. Experimental investigation on the dynamic mechanical properties of soft magnetic entangled metallic wire material. Smart Mater Struct 2017;26(5):055019.
[25] Ma Y, Hu W, Zhang D, Zhang Q, Hong J. Tunable mechanical characteristics of a novel soft magnetic entangled metallic wire material. Smart Mater Struct 2016;25(9):095015.
[26] Ma Y, Scarpa F, Zhang D, Zhu B, Chen L, Hong J. A nonlinear auxetic structural vibration damper with metal rubber particles. Smart Mater Struct 2013;22(8):084012.
[27] Tang Y, Lin G, Han L, Qiu S, Yang S, Yin J. Design of hierarchically cut hinges for highly stretchable and reconfigurable metamaterials with enhanced strength. Adv Mater 2015;27:7181.
[28] Gatt R, Mizzi L, Azzopardi J I, Azzopardi K M, Attard D, Casha A, et al. Hierarchical Auxetic Mechanical Metamaterials. Sci Rep 2015;5:8395.
[29] Lee J H, Singer J P, Thomas E L. Micro-/Nanostructured Mechanical Metamaterials. Adv Mater 2012;24:4782
[30] Nouh M, Aldraihem O, Baz A. Wave propagation in metamaterial plates with periodic local resonances. J Sound Vib 2015;341:53-73.
[31] Oudich M, Senesi M, Assouar M B, Ruzzene M, Sun J H, Vincent B, et al. Experimental evidence of locally resonant sonic band gap in two-dimensional phononic stubbed plates. Phys Rev B. 2011;84(16):165136.
[32] Hewage T A, Alderson K L, Alderson A, Scarpa F. Double-Negative Mechanical Metamaterials Displaying Simultaneous Negative Stiffness and Negative Poisson's Ratio Properties. Adv Mater 2016;28(46):10323-10332.
[33] Tran H C, Lee J. Advanced form-finding of tensegrity structures. Compos Struct 2010;88(3-4):237-246.
[34] Barnes M R. Form Finding and Analysis of Tension Structures by Dynamic Relaxation. Int J Space Struct 1977;14(2):89-104.
[35] Fraternali F, Carpentieri G, Amendola A. On the mechanical modeling of the extreme softening/stiffening response of axially loaded tensegrity prisms. J Mech Phys Solids 2015;74:136-157.
[36] Zhang D, Scarpa F, Ma Y, Boba K, Hong J, Lu H. Compression mechanics of nickel-based superalloy metal rubber. Mater Sci Eng A-Struct Mater 2013;580(37):305-312.
[37] Yang H, Wen F, Wang L, Singh S N. Newton-Downhill algorithm for distribution power flow analysis. Power and Energy Conference 2008, Pecon 2009:1628-1632.
[38] Parsopoulos K E. Particle Swarm Methods. Handbook of Heuristics 2016.
[39] Rao S S. Vibration of continuous systems. John Wiley & Sons 2007.
[40] Amendola A, Carpentieri G, Oliveira M D, Skelton R E, Fraternali F. Experimental investigation of the softening–stiffening response of tensegrity prisms under compressive loading. Compos Struct 2014;117:234-243.
[41] Zhang D, Fu J, Zhang Q, Hong J. An effective numerical method for calculating nonlinear dynamics of structures with dry friction: application to predict the vibration response of blades with underplatform dampers. Nonlinear Dyn 2016:1-15.
[42] Zhang D, Xia Y, Scarpa F, Hong J, Ma Y. Interfacial contact stiffness of fractal rough surfaces.

Sci Rep 2017;7:12874.